Single spin-polarized Fermi surface in $SrTiO_3$ thin films

Eduardo B. Guedes,[1,2,*] Stefan Muff,[1,2,*] Mauro Fanciulli,[1,2,†] Andrew P. Weber,[1,2] Marco Caputo,[1,2] Zhiming Wang,[3] Nicholas C. Plumb,[2] Milan Radović,[2] and J. Hugo Dil[1,2]

[1]*Institut de Physique, École Polytechnique Fédérale de Lausanne, CH-1015 Lausanne, Switzerland*

[2]*Photon Science Division, Paul Scherrer Institut, CH-5232 Villigen, Switzerland*

[3]*Key Laboratory of Magnetic Materials and Devices, Ningbo Institute of Materials Technology and Engineering, Chinese Academy of Sciences, Ningbo 315201, People's Republic of China*

(Received 4 September 2019; revised 25 May 2020; accepted 2 July 2020; published 31 July 2020)

The 2D electron gas (2DEG) formed at the surface of $SrTiO_3$(001) has attracted great interest because of its fascinating physical properties and potential as a novel electronic platform, but up to now has eluded a comprehensible way to tune its properties. Using angle-resolved photoemission spectroscopy with and without spin detection, we here show that the band filling can be controlled by growing thin $SrTiO_3$ films on Nb-doped $SrTiO_3$(001) substrates. This results in a single spin-polarized 2D Fermi surface, which bears potential as a platform for Majorana physics. Based on our results, it can furthermore be concluded that the 2DEG does not extend more than two unit cells into the film and that its properties depend on the amount of SrO_x at the surface and possibly the dielectric response of the system.

DOI: 10.1103/PhysRevResearch.2.033173

I. INTRODUCTION

Transition metal oxides are expected to play an important role in next generation electronics and devices, primarily driven by the interplay of lattice, charge, orbit, and spin degrees of freedom in these materials in combination with correlation effects [1]. A prominent sub-class are the titanates with a perovskite structure ($ATiO_3$) which, despite having a large band gap in the bulk, at interfaces with other materials (or vacuum), develops a high mobility two-dimensional electron gas (2DEG) with a wide variety of intriguing properties [2–5]. Especially $SrTiO_3$ (STO) has been extensively studied, partly because it was the first system where such a 2DEG was observed [6] and partly because it is an easily accessible material.

Angle-resolved photoemission spectroscopy (ARPES) is the most direct technique to access the electronic structure of materials. From comparison of experiments using soft x-ray and VUV radiation it has become clear that there is a close connection between 2DEGs found at interfaces and those found at surfaces, although the different environment will cause subtle differences in the electronic structure [7–9, and references therein]. In summary, the 2DEG consists of two circular mainly $3d_{xy}$-derived states with clear 2D characteristics and low effective mass ($m^* = 0.65m_e$), and ellipsoidal $3d_{xz}$- and $3d_{yz}$-derived states with much higher effective mass ($m^* = 15m_e$) and 3D-like dispersion [Fig. 1(a)]. The formation of the 2DEG is most likely related to a combination of oxygen vacancies, structural distortions, and a confining potential at the surface, while its population in addition strongly dependents on light-induced effects [10–13]. More recently, ARPES measurements on STO film grown by molecular beam epitaxy (MBE) suggested that the formation of the 2DEG correlates with the SrO surface termination [14], while previous *ab initio* calculations also indicated that an SrO-terminated surface favors charge accumulation [15].

Another promising aspect of the systems described above has been the discovery of a gate-tuneable Rashba-type effect with a Rashba parameter $\alpha = 3.4 \times 10^{-12}$ eV m for the 2DEG at $LaAlO_3$/STO (LAO/STO) interface [16], while $LaTiO_3$/STO interfaces have shown a larger splitting of 1.8×10^{-11} eV m [17]. For the 2DEG at the $SrTiO_3$(001) surface, an even larger $\alpha = 5 \times 10^{-11}$ eV m was found by spin- and angle-resolved photoemission spectroscopy (SARPES) [18]. The latter shows a helical Rashba-like spin texture in addition to a Zeeman-like gap around the surface Brillouin zone (SBZ) center. The exact nature of this observation and the relative contributions of magnetic order and spin-orbit interaction are still under debate [19,20]. A further SARPES measurement under different conditions failed to reproduce the finding [21], most likely due to the chosen experimental parameters (see Appendix A 6 for details).

The proposed presence of both Rashba and Zeeman interactions leads to a spin gap Δ at the Brillouin zone center of STO [Fig. 1(a)], promising a wide range of functionalities depending on where the chemical potential is placed. An interesting scenario occurs when the chemical potential is placed inside the Zeeman gap, in which case the system would show only one helical Fermi surface and resemble the situation required to form Majorana bound states [22]. Especially given the presence of superconductivity in both bulk STO [23] and STO interfaces [2,3], a whole new realm of physics opens up

[*]These authors contributed equally to this work.

[†]Present address: LPMS, CY Cergy Paris Universit, 95031 Cergy-Pontoise, France.

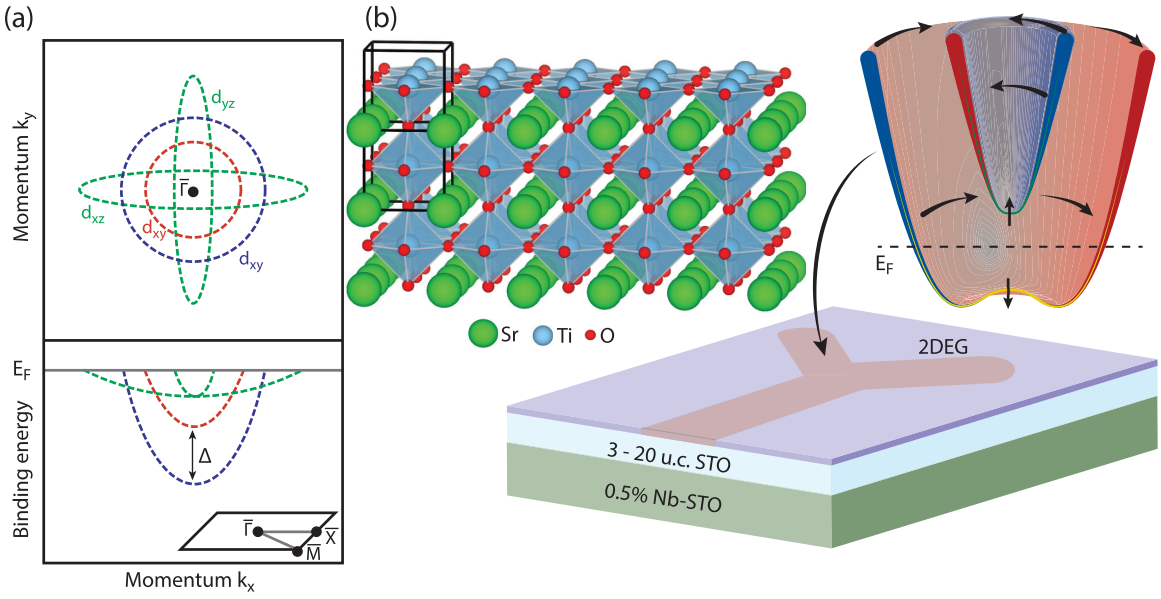

FIG. 1. The spin-polarized 2DEG on $SrTiO_3$ crystals and thin films. (a) Schematics of the electronic structure of the 2DEG on STO crystals, consisting of two circular $3d_{xy}$-derived states (red and blue) and ellipsoidal $3d_{xz}$- and $3d_{yz}$-derived states (green), where Δ represents the spin gap at the Brillouin zone center of STO. The inset shows the cubic surface Brillouin Zone. (b) Illustration [24] showing the crystal structure of STO and the STO film grown on 0.5 wt% Nb-doped STO substrate, along with the band structure of the hosted 2DEG. In this case, the Fermi level lies in the Zeeman gap at the SBZ center, thus resulting in a single spin-polarized 2D Fermi surface. This band structure, along with the superconducting properties of STO, makes this material interesting for applications and a possible 2D Majorana platform, represented by the Y-shaped pattern.

based on the interplay of magnetism, spin-orbit interaction, and superconductivity in a single material.

As indicated above, the functionality mostly relies on the possibility to shift the chemical potential while not altering other properties. In semiconductor and oxide based devices, a common approach to realize this shift is to use a gate voltage. However, the magnitude of the Rashba-type spin splitting of the 2DEG at the LAO/STO interface changes upon gating [16], and it is unclear whether such an approach can be used to tune the band filling of the 2DEG at the STO(001) surface. Remarkably, under UV light, the 2DEG hosted by this surface shows a multiband electronic structure with almost identical carrier density, irrespective of whether the sample is prepared by cleaving [10,11] or *in situ* annealing [12]. It was later shown that the band filling of the 2DEG on STO films strongly depends on the surface termination, exemplified by TiO_2-enriched [25] or SrO-terminated [14] $SrTiO_3$ surfaces, whereas the 2DEG on fractured La-doped STO crystals has been shown to respond when exposed to O_2 [13]. Further, the band structure and carrier density of fractured STO crystals can be tuned during the irradiation by UV light [11], while the 2DEG formed on nominally TiO_2-terminated STO wafers only shows a sharpening of the ARPES signal without observable changes in the band filling [12]. Whenever the carrier density was successfully tuned, it was determined *a posteriori* [11,13] and in some cases required intensive surface treatments [25].

In this work, we establish a committed approach to tailor the chemical potential, utilizing pulsed laser deposition (PLD) to homoepitaxially grow thin $SrTiO_3$ films on nominally TiO_2-terminated Nb-doped $SrTiO_3$(001) substrates. Importantly, we show that the position of the Fermi level and thus band filling varies with the amount of Nb dopants in the substrate. The similarities of the 2DEG found for films grown on 0.5 wt.% Nb-doped substrates with different thicknesses (3 to 20 unit cells) indicate that the difference between single crystals and films is not due to finite size effects. Further, we found that the 2DEG on these films have the band filling such that the Fermi level lies exactly in the Zeeman gap at the SBZ center, thus resulting in a single spin-polarized 2D Fermi surface [Fig. 1(b)]. This band structure, along with the superconducting properties of STO, makes this material interesting for applications and a possible 2D Majorana platform, represented by the Y-shaped pattern.

II. RESULTS

A. Films on highly doped substrate

The ARPES experiments were performed at the surface and interface spectroscopy beamline of the Swiss Light Source with the sample held at a temperature below 20 K. At initial exposure of the sample to the beam, we do not observe any intensity at the Fermi level. During the exposure, we note that parabolic states start to develop with a continuous increase in signal intensity. In contrast to other systems [11,13,14], we observe no shift of the band position but only an increase in intensity. All the following data were acquired after saturation of the signal.

The data for the 3, 5, and 20 u.c. STO films on 0.5 wt% Nb-doped STO substrate show marked differences to what is typically obtained for STO single crystals [10–12]. The Fermi surfaces shown in Figs. 2(a)–2(c), measured with circularly polarized light (C^+) with 85 eV, show a circular shape around the Γ points, without signatures of the ellipsoidal d_{xz}- and

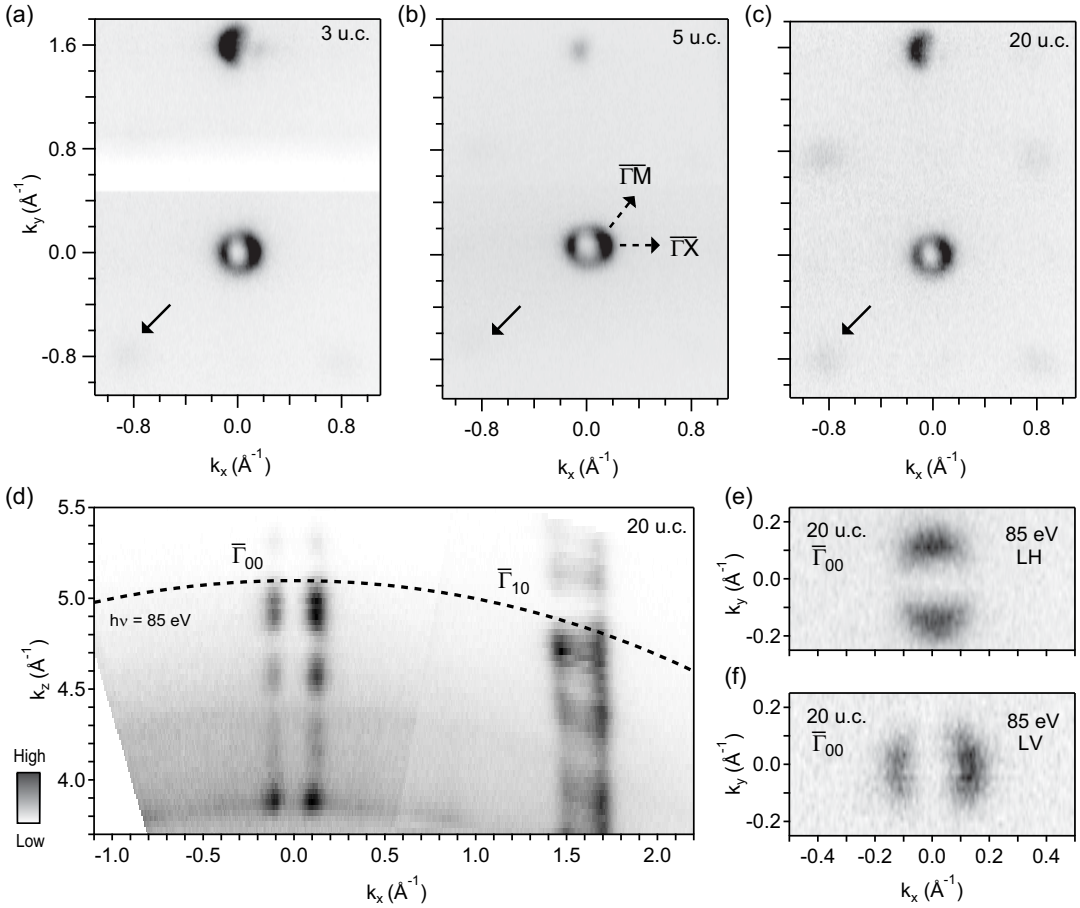

FIG. 2. 3D Fermi surface mapping of state at $SrTiO_3$ film surfaces. [(a)–(c)] Fermi surfaces of 3, 5, and 20 u.c. films grown on the 0.5 wt% Nb-doped substrate, measured at $h\nu = 85$ eV with circularly polarized light (C^+) covering $\overline{\Gamma_{00}}$ and $\overline{\Gamma_{01}}$ as well as reconstructed Γ points, indicated by arrows. The lack of signal in (a) at $k_y = 0.5$ Å^{-1} is due to a synchrotron beam loss. (d) Dispersion with k_z for the 20 u.c. sample along $\overline{\Gamma X}$. [(e) and (f)] Zoom of FS with linear-horizontal (LH) and linear-vertical (LV) polarizations.

d_{yz}-derived states for any of the three film thicknesses. The absence of these states is verified with the 20 u.c. film in the photon energy scan (i.e., dispersion along k_z, calculated using an inner potential $V_0 = 14.5$ eV [12]), shown in Fig. 2(d), which shows a pure 2D character. The observed intensity variations are due to the $3p$–$3d$ resonance at around $h\nu = 45$ eV ($k_z \approx 3.8$ Å^{-1}) and Bloch spectral enhancement at bulk Γ points [26]. Further, that the 2DEG is d_{xy}-derived can be seen by dependence of the Fermi surface with light polarization (linear vertical and horizontal, LV and LH), which in our experimental geometry is a signature of a band with d_{xy} character [Figs. 2(e) and 2(f)].

As evident also in their RHEED pattern (see Appendix A 1), we observe band foldings along the ΓM direction in all the Fermi surfaces with varying clarity, indicated by the solid arrows in Fig. 2. Such folded bands are signatures of a $\sqrt{2} \times \sqrt{2}$R45° surface reconstructions, which has been assigned to the presence of SrO at the STO surface [27]. Despite their visibility in the ARPES spectra, the bands around the reconstructed $\overline{\Gamma}$ points are relatively featureless. This suggests that the reconstruction is not long range ordered, and thus was not considered in the following analysis. Finally, there is no sign of the heavy bands for any of the studied films, thus all the samples host a purely d_{xy}-derived 2D state (for details, see Appendix A 3).

A close comparison of the band structures of the 3, 5, and 20 u.c. STO films on 0.5 wt% Nb-doped STO substrate shows very similar Fermi surfaces [Figs. 3(a)–3(c)] and band dispersions [Figs. 3(d)–3(f)]. There is no noticeable change in Fermi wave vector k_F [Fig. 3(j)], and the formation of the valence band [Fig. 3(k)] and the in-gap state [Fig. 3(l)] are also similar for the three films. In the 2D curvature [Figs. 3(g)–3(i)] [28] and in the k_x integrated EDCs [Fig. 3(m)], polaron replicas of the d_{xy} band with an energy separation of ≈100 meV are visible, indicated by arrows. These are large polarons formed in the photoemission process commonly observed in titanates [25,29]. It is also worth noting the intense incoherent spectral weight at the center of the SBZ that appears below 150 meV, also often observed for the 2DEG on STO crystals [10–12].

The fact that no differences are observed as a function of film thicknesses rules out the influence of finite size effects and constrains the spatial extension of this 2DEG from the top TiO_2 layer to 2 u.c. or less into the film, and further hints at an origin beyond a simple band bending model [10,30]. The 2D curvature data show the shape of the d_{xy} band that follows a free-electron-like dispersion. The parabola plotted

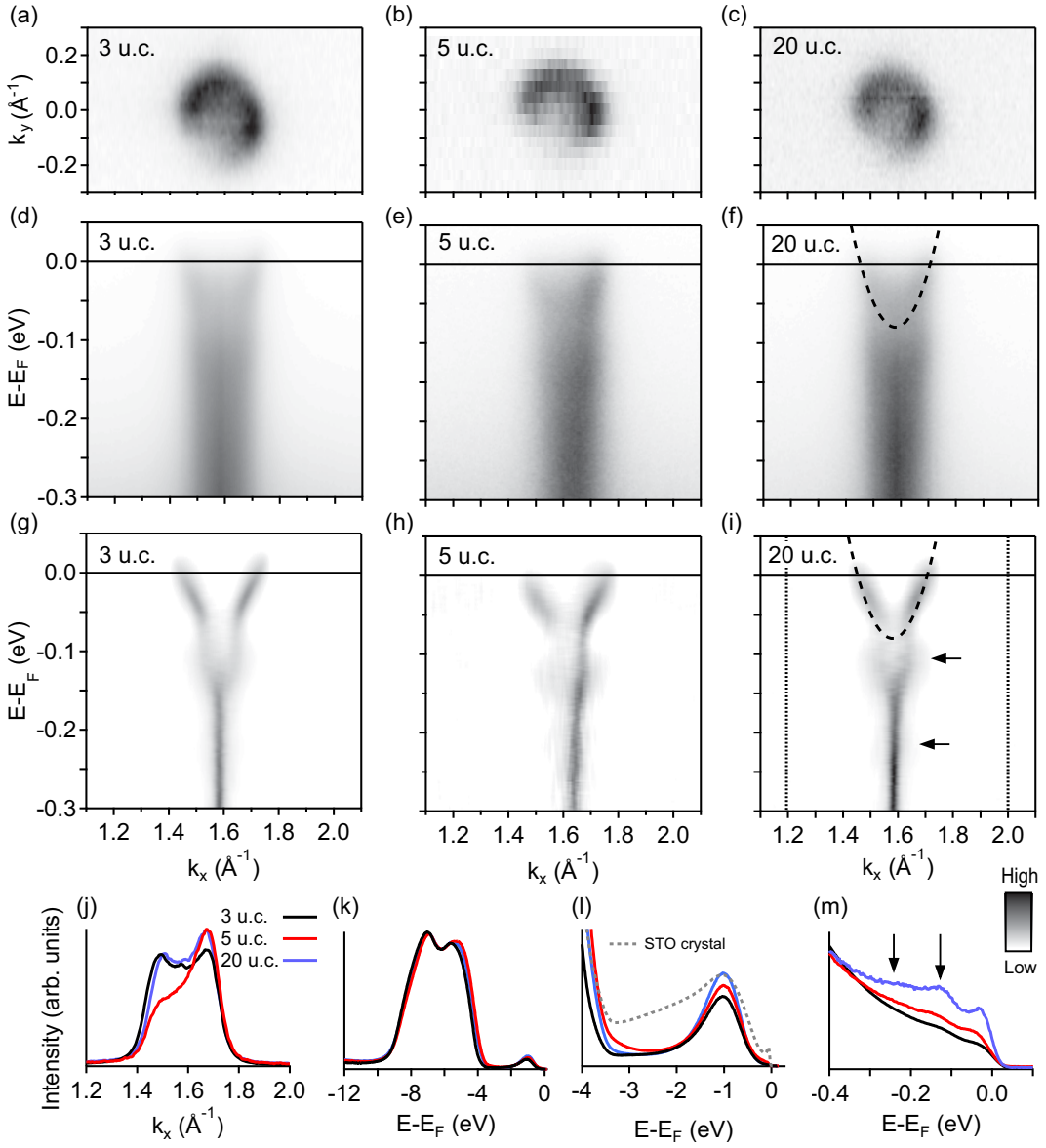

FIG. 3. The 2DEG on 10 u.c. film grown on highly doped substrate. (a) Fermi surface, (b) band structure and (c) 2D curvature for 3 u.c. STO on the 0.5 wt% Nb-doped substrate at $\overline{\Gamma_{10}}$ with $h\nu = 85$ eV (C^+). (b), (e), (h) and (c), (f), (i) same as (a), (d), (g) but for 5 u.c. and 20 u.c., respectively. A free electron-like parabola is indicated in (f) and (i). (j) MDCs of the three films at the Fermi energy from (d), (e), and (f). (k) Valence band EDCs integrated along k_x, (l) the in-gap state, (m) zoom around the Fermi level showing the polaron replicas (arrows). The spectrum of a STO single crystal is shown for comparison in (l).

in Figs. 3(f) and 3(i), with a band bottom of 80 meV and an effective mass of $m^* = 0.74m_e$, matches well the observed dispersion of the three samples. Furthermore, the small increase in effective mass ($m^* = 0.65m_e$ for the 2DEG on STO single crystals [12]) points to an altered bond angle, likely due to surface relaxation. Due to the absence of the heavy d_{xz}/d_{yz} bands, it cannot be confirmed whether the splitting between these and the d_{xy} band has changed.

In addition to the reduced band filling, the in-gap states observed in our thin films are different from the ones observed in the bulk counterpart [Fig. 3(l)]. For single-crystal STO (dashed line), two in-gap states are observed whereas for the STO films the state at 2.5 eV binding energy has disappeared. Both in-gap states are known to originate from defects [31,32]. The different in-gap states suggests a different defect structure of our PLD-grown STO films when compared to STO crystals.

Apart from the likely small change in bond angle, the most striking difference of the 2DEG found on our STO/Nb:STO films when compared to the universal 2DEG found in cleaved and annealed STO crystals [10–12] is the large reduction of band filling from 230 to 80 meV. This corresponds to a downwards shift of the Fermi level, which now is crossed by a single band (Fig. 3). Considering the spin texture measured for the 2DEG on the surface of bulk STO [18], applying a rigid upwards energy shift would lead to a single spin-polarized Fermi surface. However, given the general differences of thin films, a change in spin splitting cannot be excluded

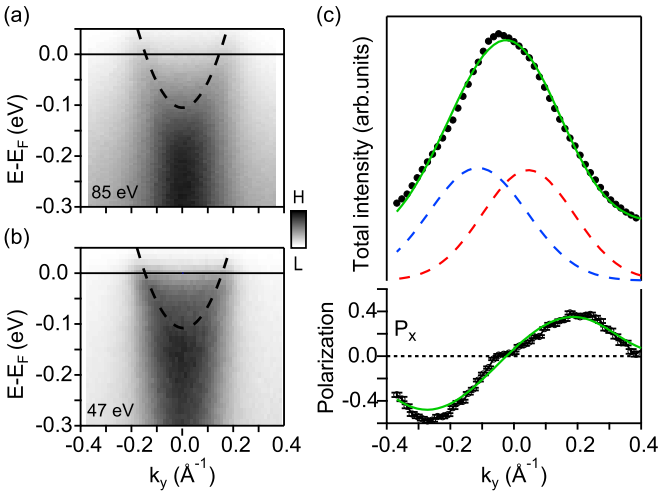

FIG. 4. Spin-polarization of single band at Fermi level. Electron dispersion of 10 u.c. STO film grown on 0.5 wt% Nb:STO with (a) $h\nu = 85$ and (b) 47 eV. (c) Spin-resolved MDCs at the Fermi level and respective P_x spin polarization The solid green lines are results of the simultaneous fit of total intensity and spin-polarization.

and requires experimental verification. In order to access this often elusive degree of freedom, we employed spin-resolved ARPES to study a 10 u.c. STO/0.5 wt% Nb:STO film, well within the previously studied 3–20 u.c. range.

Figure 4 shows the spin-integrated band dispersion measured at the COPHEE end-station [33] for a 10 u.c. STO/0.5 wt% Nb:STO film, along the $\overline{\Gamma Y}$ direction, with C^+ photons of 85 eV and 47 eV [Figs. 4(a) and 4(b)]. Although the observed bottom of the d_{xy} band in these measurements are 20 meV lower than in the spin-integrated data of Fig. 3, the spectra still shows only one band, well described by the same parabola as in Fig. 3 when the 20 meV shift is taken into account (dashed line). The spin-resolved MDC measured with $h\nu = 85$ eV photons at the Fermi level is shown in Fig. 4(c). The main spin polarization signal points along the x direction, while the measured out-of-plane spin polarization is most likely due to spin interference during the photoemission process [34] and $|P_y| \leqslant 0.04$ (see Appendix A 5 for details).

A well-established routine [35] was used to simultaneously fit the total intensities and the spin polarization data. The fitted total intensity and polarization along the sample x direction (P_x) are represented by green solid lines in Fig. 4(c), while the red and blue dashed lines represent the individual peaks of the fit. The spectrum around $\overline{\Gamma}_{10}$ originates from a single band whose polarization is perpendicular to the crystal momentum and reverses sign at the SBZ center, consistent with a helical spin texture as also observed for the 2DEG on STO crystals [18]. Hence, the Fermi level for the films grown on 0.5 wt% Nb-doped STO(001) substrate (Fig. 3) lies inside the Zeeman gap and the electronic structure thus show a single spin-polarized Fermi surface.

B. Films on low-doped substrate

In order to further explore the 2DEG developed on PLD-grown STO/Nb:STO(001) films, we grew 10 u.c. films on 0.05 wt.% substrates, i.e., where the amount of Nb dopants is changed by one order of magnitude. Figure 5(a) shows the k_z dispersion around $\overline{\Gamma}_{10}$ for this film. As for the films on the low-doped substrate, here the heavy bands are not observed either. Figure 5(b) shows a Fermi surface obtained with 47 eV photons with C^+ polarization, where a circular outer band with $k_F = 0.18$ Å^{-1} is evident, along with an increase in intensity towards the center, indicated by an arrow. The band dispersion measured at $k_y = 0$ Å^{-1} [Fig. 5(c)] and the respective curvature analysis [Fig. 5(d)] [28] reveals a band filling of around 170 meV. Again relying on the 2DEG on STO crystals, a rigid band shift of the outer d_{xy} band from the 230 meV to the 170 meV would result in an inner d_{xy} band populated up to ≈40 meV, with $k_F \approx 0.05$ Å^{-1}. Indeed, spectral weight can be seen at E_F around $k_x \approx 1.55$ Å^{-1} in Fig. 5(d), indicated by an arrow, although a clear band dispersion could not be fully resolved. Despite this uncertainty, which inspires further investigation with other differently doped substrates, it is clear that this film also does not show the heavy bands and hosts distinct (similar) in-gap states as crystals (films on highly doped substrates) [Fig. 5(f)].

C. X-ray photoelectron spectroscopy of core levels

Our results raise the question why PLD-grown STO films on Nb:STO substrates show a smaller band filling. Further information can be gathered from a detailed analysis of Ti $3p$ and Sr $3d$ core levels, shown in Fig. 6, measured with $h\nu$= 170 eV. In Fig. 6(a), the Ti $3p$ core level of the 20 u.c. film grown on the 0.5% Nb:STO substrate, measured at normal emission (NE), shows the typical Ti^{4+} peak (which comprises the Ti $3p_{3/2}$ and Ti $3p_{1/2}$ contributions), followed by a Ti^{3+} shoulder. Figure 6(b) shows a fit of this data, evidencing the two components and allowing a quantitative analysis of the spectrum. The increase in Ti^{4+}/Ti^{3+} ratio in the data measured with an emission angle of 45° shows that the Ti^{3+} is mostly located at the surface of the sample, as previously observed [12]. For comparison, in Fig. 6(a), we show the spectrum of a STO crystal, which is similar to the 20 u.c. film, apart from a broader Ti^{3+} component. All the films studied in this work present Ti $3p$ core levels with similar line shapes, and although the Ti^{3+} content varies from sample to sample, it does not seem to show a systematic evolution with the Nb content or thickness (details in Appendix A 7).

The Sr $3d$ spectrum of the 20 u.c. film measured at NE [Fig. 6(c)] also shows a two-component shape, which is decomposed in Fig. 6(d) including the $3d_{5/2}$ and $3d_{3/2}$ components. The spectrum measured at and emission angle of 45° confirms that the component at higher binding energy is mostly located at the surface of the sample, and is typically attributed to the formation of SrO_x crystallites [36]. Furthermore, an elemental analysis of the XPS spectra reveals that the Sr/Ti ratio in our films is between 1–1.20, while the crystals we studied show a ratio of ≈1.40. These values are consistent with what was reported recently for MBE films grown with different terminations [14].

Comparing the Sr $3d$ spectrum of the 20 u.c. film with the one of a STO crystal, also shown in Fig. 6(c), we observe not only an increase in intensity of the surface Sr contribution, but also an energy shift of about 200 meV towards higher

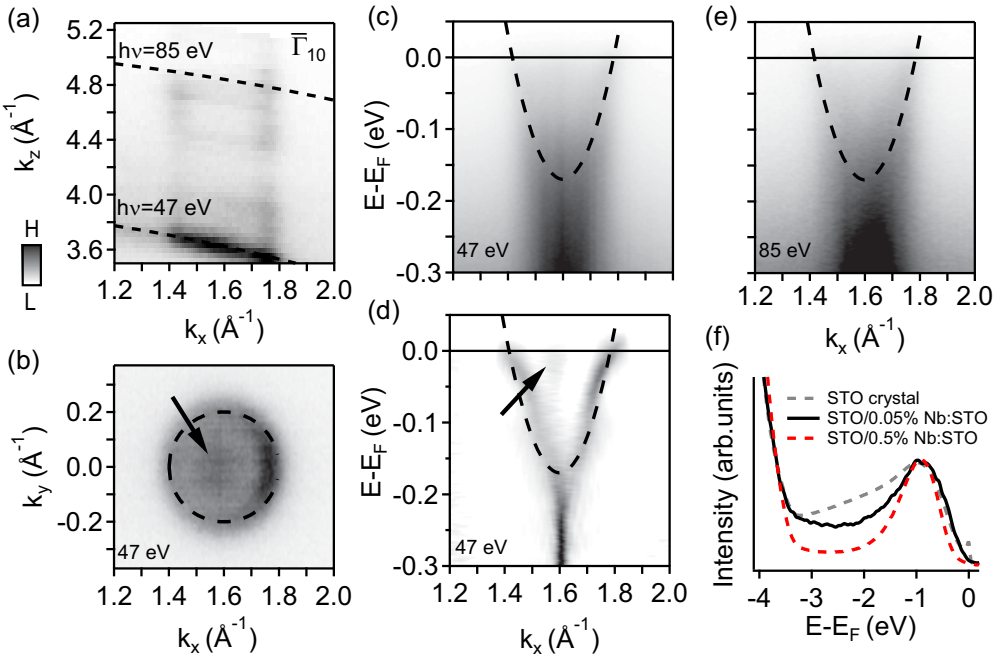

FIG. 5. The 2DEG on film grown on low-doped substrate. (a) Fermi surface in the k_x-k_z plane and (b) k_x-k_y plane of 10 u.c. STO film grown on 0.05 wt% Nb:STO. (c) Band dispersion along $\overline{\Gamma X}$ measured with $h\nu = 47$ eV and the respective second derivative analysis (d). (e) Band dispersion along $\overline{\Gamma X}$ measured with $h\nu = 85$ eV. (f) EDC of the in-gap states, where the spectrum from a STO crystal is shown for comparison.

binding energy. Additionally, the surface Sr signal appears to be almost independent of film thickness, as seen in Fig. 6(e), where the 3, 5, and 20 u.c. films show very similar spectra. In particular, the spectrum for 5 u.c. shows a slightly smaller surface Sr contribution, although the peak position matches well the ones of the 3 and 20 u.c. films. For further comparison, Fig. 6(e) also presents the Sr 3*d* spectrum of the 10 u.c. 0.05% Nb:STO film, which differs from the films on the highly doped substrate, and more closely resembles the one from STO crystals [Fig. 6(c)].

We now recall that the filling of the $3d_{xy}$ band varies from crystals to films with either doping, although the amount of Ti^{3+} is similar in all samples. This indicates that there is no direct correlation between the amount of Ti^{3+} with the band

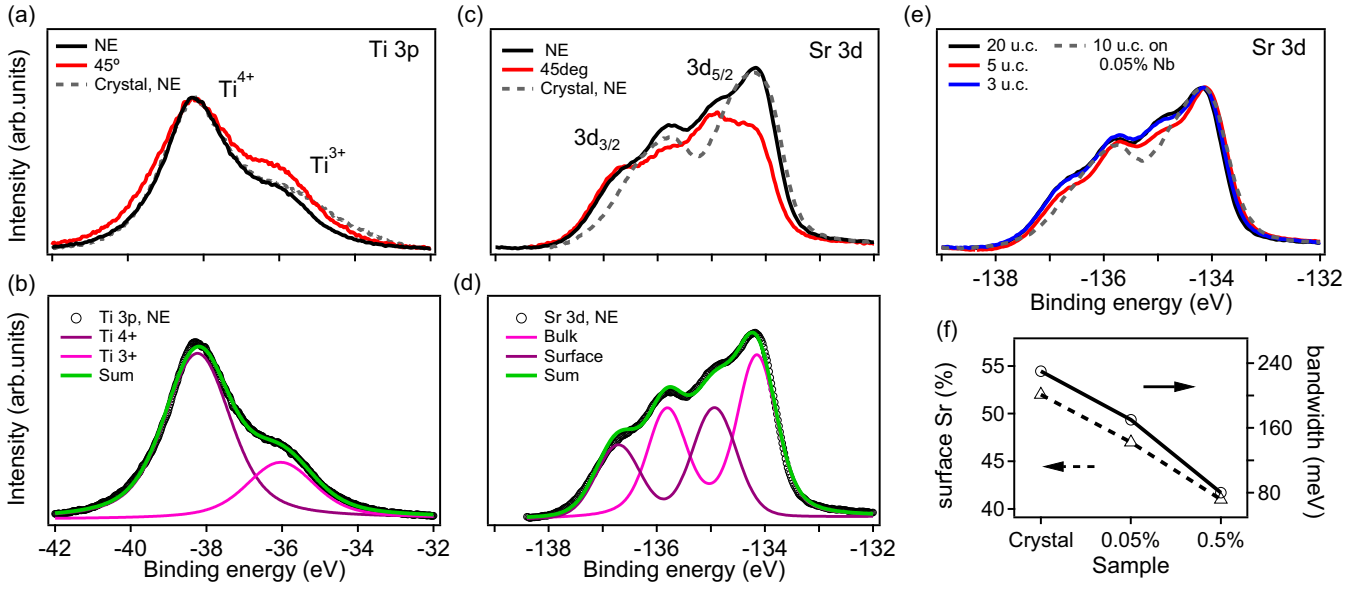

FIG. 6. XPS analysis of PLD-grown STO films. (a) Ti 3*p* core level measured at normal emission (NE) and 45°, as well as the spectrum of a STO crystal measured at NE, (b) fit of the spectrum of the film at NE. [(c) and (d)] The equivalent dataset for Sr 3*d* core level. (e) Comparison of the Sr 3*d* core level of films of different thicknesses and substrates. (f) Correlation between band filling and the magnitude of the surface Sr contribution.

filling of the 2DEG, likely due to the fact that the extra charges in STO not only form a 2DEG, but also remain localized around defects and show up as the in-gap states [Figs. 3(l)] [37,38]. In turn, the shape of the Sr 3*d* spectra and the amount of SrO_x crystallites shows a trend when compared to the observed band filling, as seen in Fig. 6(f). Whether this observation fully explains the differences in band filling requires further investigation with microscopy and spectromiscroscopy techniques [39].

As mentioned previously, the observed differences regarding the in-gap states suggest that defects present in our thin films are different than those in STO crystals. In fact, this may be another reason for the change in band filling from wafers to thin films, since a different defect structure leads to a different dielectric response of each system. This, in turn, is expected to alter the properties of the polaronic excitations and thus the band characteristics [40]. Optical and spectroscopic measurements have shown that the dielectric response of $SrTiO_3$ changes from single crystals to thin films [41,42], which can ultimately impact the electronic confinement and the observed band filling. In this respect, it is important to note that the MBE grown films on 0.05% Nb-doped substrates [14] show a band bottom at around 170 meV, which is comparable to our results on PLD films grown on similar substrates. The above hypothesises about the influence of SrO_x at the film surface and the altered dielectric response are not mutually exclusive and may indeed be closely related.

III. DISCUSSION AND CONCLUSIONS

As indicated above, we found that the band filling for the film grown on the 0.5% Nb:STO substrate is such that the chemical potential lies inside the Zeeman gap, leading to a single spin-polarized band [Fig. 1(b)]. In practice, this result hints that local gating of the substrate can be used to create wires at whose tips zero bias anomalies might be observable by tunneling experiments. Alternatively the wires can also be written by illuminating with an intense light source, by local defect doping, or by writing with a conductive tip [43]. In combination with the superconducting properties of STO, this unifies all the ingredients for the formation of Majorana bound states in a single material without the need of external fields.

The indication that the doping level of the substrate can influence the band filling of the 2DEG—and not in a trivial manner, since the higher the doping level in the substrate, the smaller the band filling—inspires further systematic and detailed study. If shown to be true, this would allow to tune the 2DEG on STO in a very stable way, and open the way to prepatterning the substrate, enabling the growth of regions with different band filling (and topology).

ACKNOWLEDGMENTS

This work was supported by the Swiss National Science Foundation (SNF) Project No. PP00P2_144742 and No. PP00P2_170591. M.R. and E.B.G. acknowledge the support of SNF Project No. 200021_182695. Z.W. was supported by the National Natural Science Foundation of China under Project No. 11874367.

APPENDIX: SUPPORTING INFORMATION

1. Growth of the films

The $SrTiO_3$ thin films were grown by pulsed laser deposition (PLD) on commercially available, single TiO_2 terminated 0.05 and 0.5 wt% Nb-doped STO(001) substrates (Twente

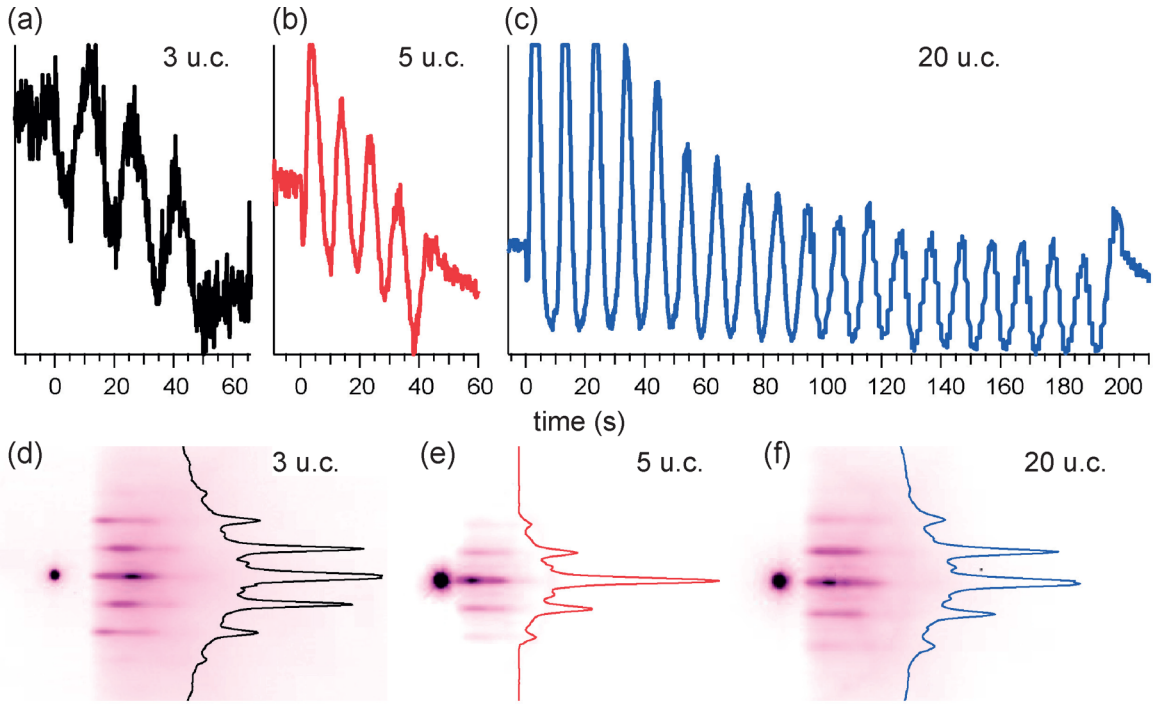

FIG. 7. RHEED oscillations of the film growth of (a) 3 u.c., (b) 5 u.c., and (c) 20 u.c. STO on 0.5 wt% Nb:STO(001) substrates. [(d)–(f)] RHEED patterns of the three films after the growth at the growth temperature, along with the intensity line profiles.

Solid State Technology), using a crystalline STO disk as target. The reflection high-energy electron diffraction (RHEED) oscillations used to control the thicknesses of 3, 5, and 20 u.c. films on 0.5 wt% Nb-doped STO(001) are displayed in Figs. 7(a)–7(c). The RHEED patterns recorded after the growth show straight lines indicating a flat, 2D film surface. Between the main diffraction intensities, low intensity lines are visible [Figs. 7(d)–7(f)]. It is interesting to note that the RHEED intensity actually increases with the growth of the first overlayer of STO on the substrate, indicating the high quality of the films.

2. Details of (S)ARPES measurements

The prepared films were transferred *in situ* to the high-resolution ARPES endstation at the Surface and Interface Spectroscopy beamline of the Swiss Light Source at the Paul Scherrer Institut. X-ray photoemission (XPS) and ARPES spectra were measured with a Scienta R4000 analyzer with instrumental angle and energy resolution better than 0.2° and 10 meV. In order to perform spin-resolved ARPES, new films were grown and transferred in a vacuum suitcase under ultrahigh vacuum conditions to the COPHEE endstation [33], which uses an Omicron EA 125 hemispherical energy analyser and two orthogonally assembled classic Mott detectors. The angle and energy resolutions of the SARPES measurements are better than 1.5° and 70 meV. For all the measurements the samples were kept under pressures better than 5×10^{-10} mbar and at 20 K. No further sample treatment was required. These results were reproduced on different samples, in independent experiments.

3. Dimensionality of the 2DEG

In the photon energy scans of the 20 u.c. film shown in Fig. 2 of the main text, the d_{xy}-derived state shows a pure 2D character. This is also concluded for the 3 and 5 u.c. films as noted below. Figure 8 shows the a the Fermi surface in k_x-k_y plane for the 5 u.c. film along the high-symmetry directions ΓX and ΓM, which show a pure 2D character, with no hints of the heavy bands. Intensity variations are observed as in the 20 u.c. film presented in the main text. In particular for the ΓM direction, we observe spectral weight due to the $\sqrt{2} \times \sqrt{2}$R45° surface reconstruction, as pointed by the arrow in Fig. 8(b), as well as in the Fig. 2 of the main text. The bands around the reconstructed $\overline{\Gamma}$ points are relatively featureless, and apart from a resonant enhancement do not show the same structure as a function of photon energy as the main $\overline{\Gamma}$ points. It appears that the reconstruction is not long range ordered, and thus it was not considered in the analysis. Given the similarities of the data of the 3 u.c. film with the 5 and 20 u.c. ones, particularly the absence of the heavy bands in the spectra measured with $h\nu = 85$ eV, we conclude that the 3 u.c. film also shows a purely 2D state.

4. ARPES of films on different substrates

The larger band filling of the 2DEG on the films grown on the 0.05 wt%, compared to the ones and 0.5 wt% Nb-doped STO(001) substrate, is presented in Fig. 5 of the main

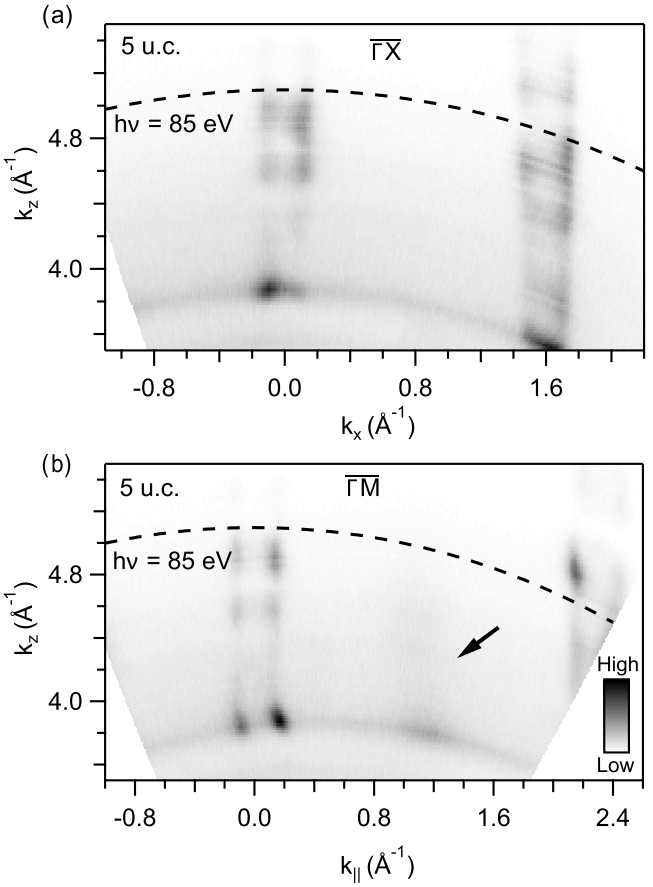

FIG. 8. 3D Fermi surface mapping of state at 5 u.c. $SrTiO_3$ film grown on the 0.5 wt% Nb-doped substrate. Along (a) $\overline{\Gamma X}$ and (b) $\overline{\Gamma X}$, with circularly polarized light covering $\overline{\Gamma_{00}}$ and $\overline{\Gamma_{10}}$. The arrow in (b) indicates the reconstructed $\overline{\Gamma}$ point.

text. Here we compare the MDCs and EDCs obtained from these two samples, to show that the data indeed suggests the presence of two bands on the film grown on the 0.05 wt% substrate, in contrast to the one band present in the film on the 0.5 wt% one.

We begin by presenting the MDC and EDC from the data of Fig. 5 of the main text, *i.e.* the 0.05% sample measured at the high-resolution endstation with 47 eV photons. The MDC shows peaks at 1.43 and 1.77 Å^{-1}, corresponding to the outer band, and a broad structure from 1.52 to 1.66 Å^{-1} [Fig. 9(a)]. In turn, the EDC in Fig. 9(b) shows bumps corresponding to the bottoms of the bands at 50 and 170 meV, marked by arrows. Note that EDCs at $k_y = 0$ Å^{-1} typically give only a low peak to background ratio in this system.

Now we discuss the EDCs and MDCs from the measurements with 85 eV photons performed at the COPHEE endstation. The MDCs at E_F are shown in Fig 9(c). The data for the 0.05% sample shows an inner structures at $k_x = -0.07$ and 0.07 Å^{-1} (marked with arrows), which are absent in the spectrum of the 0.5% sample. As for the EDCs in Fig. 9(d), despite the intense background, the data for the 0.5% sample show one structure between E_F and 100 meV (red arrow), while the 0.05% sample shows structures at 50 and 170 meV (black arrows), which correspond

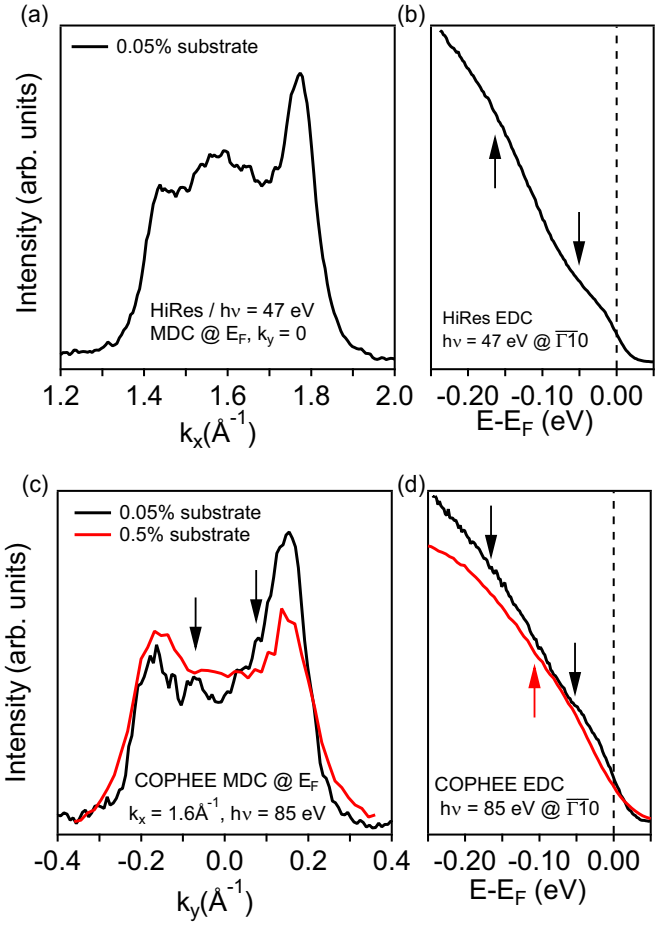

FIG. 9. Extracted (a) MDC and (b) EDC for the 0.05% sample measured at the high-resolution endstation at 47 eV, C^+ polarization. (c) and (d) shows MDCs and EDCs for the 0.5% and 0.05% Nb-doped samples measured at COPHEE with 85 eV photons, C^+ polarization.

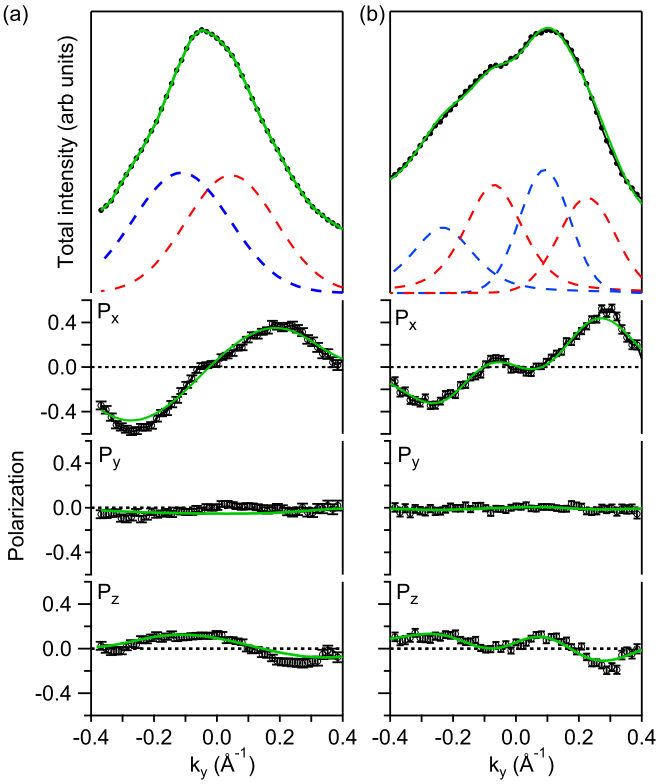

FIG. 10. Spin-polarized MDCs at the Fermi level of two 10 u.c. films on (a) 0.5 and (b) 0.05 wt% Nb-doped substrates. Each panel presents the total intensity split into the three spatial components P_x, P_y, and P_x (markers), as well as the spin-resolved MDC (dashed lines). The green lines are the result of the simultaneous fit of the total intensity and $P_{x,y,z}$.

to the bottom of the bands observed in the angle-resolved spectra.

The differences are difficult to observe in the spin-integrated data obtained at the COPHEE endstation. This is primarily because those measurements are performed using an old-fashioned channeltron detector with rather limited energy and angular resolution. The expected change in k_F for a rigid band shift of 90 meV is around 0.05 $Å^{-1}$, below its resolution limit (but above the one from the high-resolution endstation).

5. SARPES of films on different substrates

We now proceed with the comparison of the obtained spin-resolved data. Figure 10(a) shows the spin-resolved MDC of the 10 u.c. STO/0.5 wt% Nb:STO film, measured at the Fermi level with C^+ photons of 85 eV, along the $\overline{\Gamma Y}$ direction, the same as in Fig. 4(c) of the main text. As mentioned, the main spin polarization signal points along the x direction, while $|P_y| \leqslant 0.04$ and $|P_z| \leqslant 0.2$. The measured out-of-plane spin polarization is most likely due to spin interference during the photoemission process [34]. The simultaneous fit [35] of the total intensities and the spin polarizations along the sample x, y, and z axes are denoted by the green lines. The fit resulted in a pair of peaks (one band), whose spin-polarization is consistent with a Rashba-type effect. Figure 10(b) shows the equivalent data obtained for a 10 u.c. STO/0.05 wt% Nb:STO film, grown under the same conditions as the film in Fig. 5 of the main text. In this case, the data could only be fitted with four of peaks (two bands), with oppositely winding spin textures, also consistent with a Rashba-type spin texture. This observation is consistent with the possibility of the second branch of the d_{xy} band being populated, as discussed in the main text.

We further explored this film with with $h\nu = 47$ eV, vertically polarized light, measuring spin-resolved MDCs at two different binding energies $E_{1,2}$, defined in Fig. 11(a), and shown in Figs. 11(b) and 11(c). Again, for both $E_{1,2}$ the main spin polarization signal is along the x direction, and the same origin for the polarization signals in y and z directions apply to this film. For $E = E_1$, the fit resulted in two peaks with opposite spin polarization, while the spectra measured around $E = E_2$ can only be fitted assuming four peaks with alternating spin polarization.

For completeness and easy viewing we show in Figs. 12(a) and 12(b) the spin up $I^{\uparrow}$ and down $I^{\downarrow}$ spectra projected on the x axis for the data shown in Fig. 3 of the main text and Fig. 11. In Figs. 12(c) and 12(d), we show the equivalent data for the spectra presented in Fig. 11. The spectra are

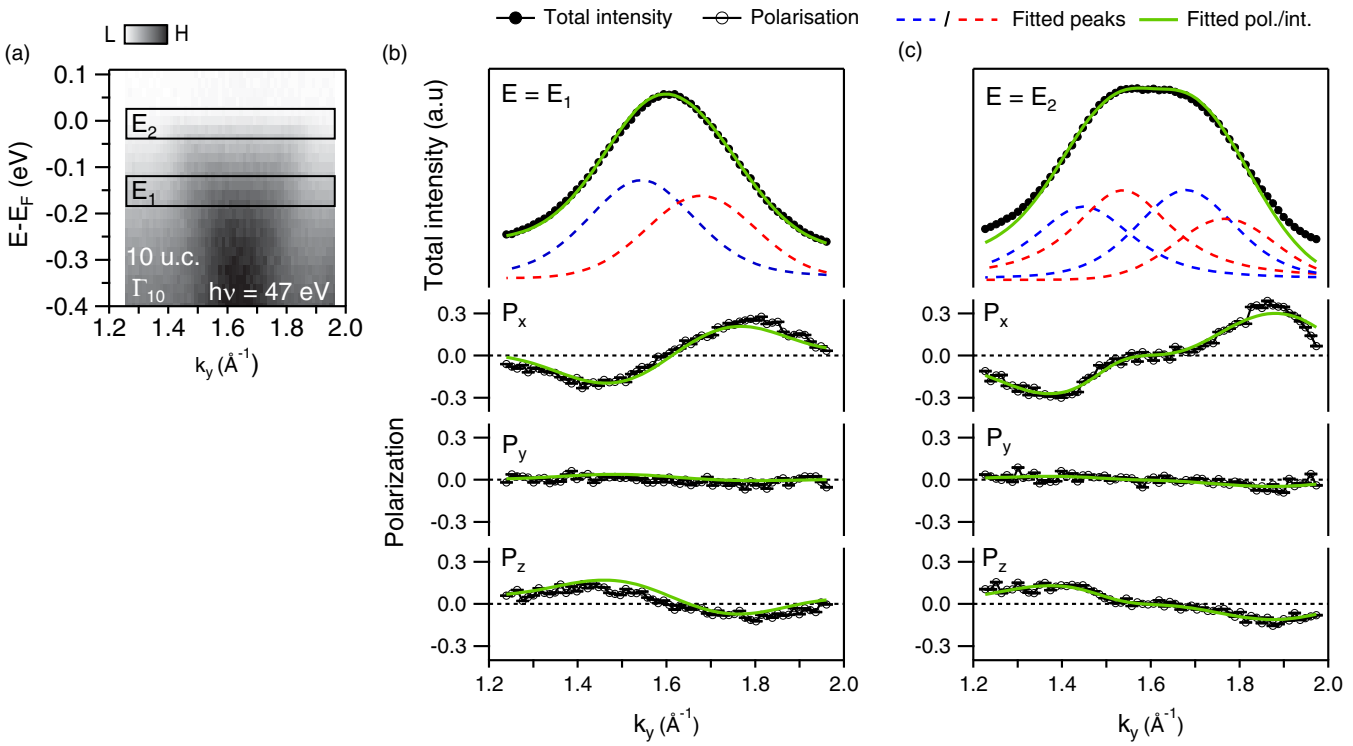

FIG. 11. Spin-polarization of the 2DEG on a 10 u.c. film on 0.05 wt% Nb-doped STO(001). (a) Spin-integrated band map measured with $h\nu = 47$ eV, LV-polarized light, and the definition of the $E_{1,2}$ energy windows. Total intensity and related $P_{x,y,z}$ spin polarizations, along with their respective fits for (b) $E = E_1$ and (c) E_2.

obtained by

$$I_x^{\uparrow,\downarrow} = \tfrac{1}{2}(1 \pm P_x) I_{\text{tot}}.$$

Here I_{tot} is the measured total intensity and P_x the measured spin polarization along the sample x axis. No further data treatment is applied and the number of peaks is easily resolved also from this graph. However, because of the projection on only a single axis, the splitting of the states and their relative intensity can be different compared to the analysis taking all three spatial components into account.

From the fact that the spin-resolved MDCs at E_F of the films on 0.5% and 0.05% substrates (Fig. 10) look similar to when we change the binding energy, going from 1 to 2 bands (Fig. 11) (as well as to STO crystals [18]), and because we see the change in band filling in the high-resolution data, we infer that the film on 0.05%Nb:STO substrate presented two bands crossing E_F. However, this claim requires further investigation with films of different thicknesses and other substrates.

6. Comparison to conflicting SARPES results

Triggered by the SARPES results on STO crystals published in Ref. [18], another group has attempted to reproduce these findings under different conditions, but found no clear spin polarization signal [21]. This discrepancy deserves attention, although a full explanation will probably require both further studies and input from the authors of Ref. [21]. First

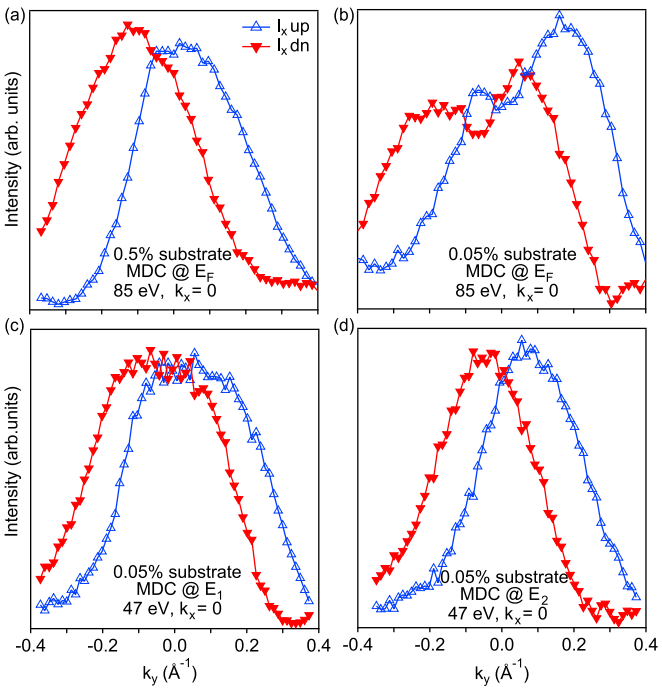

FIG. 12. Spin-polarized MDCs projected on the x axis, measured at COPHEE with 85 eV, circularly polarized light for (a) the 0.5% Nb-doped substrate at E_F; (b) for the 0.05% Nb-doped substrate at E_F; and with 47 eV, LV light (c) for the 0.05% Nb-doped substrate at E_2; and (d) for the 0.05% Nb-doped substrate at E_1.

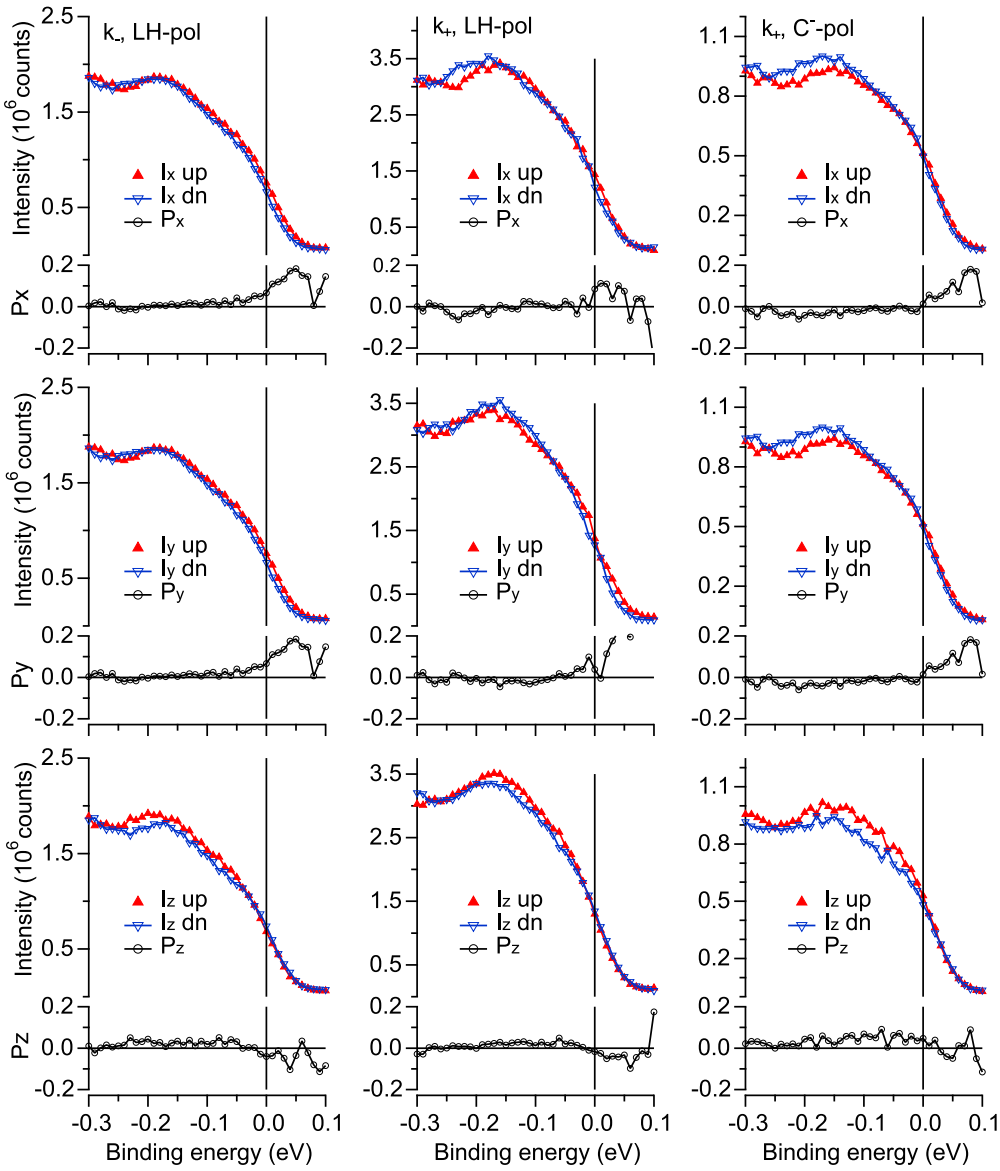

FIG. 13. Spin-polarized EDCs of measured at COPHEE with 85 eV, using the same STO crystals as in [10]. $k_{+,-}$ denotes the Fermi momenta to the left and right of $\overline{\Gamma_{10}}$.

of all, one can consider the results presented here as a further verification of Ref. [18] for a slightly different system. In both cases, the spin signal is clear in the raw data and requires no further analysis to determine the number of spin-polarized peaks. Also the obtained peak positions match well with those found for high-resolution ARPES data, which further solidifies the conclusion. That the obtained spin polarization is not an artefact of the COPHEE endstation follows from the large number of SARPES results from this machine which have been reproduced by other groups or by one-step photoemission theory. The combination of Rashba-like spin-orbit interaction and a Zeeman-like gap around the zone center are the simplest explanation of the observed spin texture, but this does not exclude the possibility of a more complex explanation.

Now let us consider the differences in Ref. [21] with respect to Ref. [18]. In Ref. [21], the samples are La-doped and cleaved, which show a different evolution under synchrotron light, as noted in the end of Sec. I [11,12]. The measurements in Ref. [21] are performed on a different SARPES endstation which uses a Mott detector that is less stable, as described in Ref. [44]. However, also this should ideally have no large influence. The most importance difference, that can most likely explain the absence of a spin signal to a large extent, is the used photon energy. In Ref. [21], a photon energy of 80 eV is used which coincides with the photon energy range where the $d_{yz,xz}$-derived heavy bands are strong and disperse to overlap with the d_{xy}-derived states for the crystal surface. Note that for the films these heavy bands are not occupied. Due to their strong 3D character these states show almost no spin polarization but they can mask the spin signal from the d_{xy}-derived states. This is also clear from the SARPES data shown in Fig. 13 obtained at $h\nu = 85$ eV at the COPHEE endstation for the STO crystal surface. These data were obtained in 2012

on the exact same samples and during the same measurement run as in Ref. [18]. Clearly no significant spin polarization signal can be distinguished also in this case.

Lastly, there are some other points in Ref. [21] that could explain the absence of a spin signal, but these would require more in-depth verification. Most importantly the data in Fig. 2(b) of Ref. [21] appear to show a highly contaminated surface and are markedly different from the data in Fig. 2(c) or what were observed in Ref. [18]. Whether under these conditions a spin signal can be expected requires further studies, but most likely the charge from adsorbates will significantly alter the properties of the 2DEG.

7. Details of the XPS analysis

The top panels of Fig. 14 shows the Sr 3*d* and Ti 3*p* XPS spectra of the STO crystal, 20 u.c. films on 0.5% Nb:STO and 10 u.c. films on 0.5% Nb:STO, along with their respective fits in the lower panes. For simplicity, we omitted the fits of spectra of the 3 and 5 u.c. films, which are only shown for comparison as dashed lines in the top panels. The XPS analysis done in the main text is based on the fits shown in Fig. 14, where each of the peaks is a convolution of the Lorentzian and Gaussian functions. A Shirley-type background was subtracted from all spectra.

For the Sr 3*d* spectra, we used two pairs of peaks (for bulk and surface components), each with a fixed ratio of 2/3 between the spin-orbit contributions. The average spin-orbit splitting of the bulk and surface Sr varied between 1.68 and 1.75 eV, with a variation smaller than 2% among the spectra. The Sr/Ti ratio, calculated taking into account the Ti 3*p* and Sr 3*d* photoionization cross-sections [45], was found to be 1.4 in the studied crystal and varies between 1–1.20 in the studied films, as described in the main text. For the Ti 3*p* spectra, two independent peaks were used, representing the Ti^{3+} and Ti^{4+} contributions. The ratio of the surface and bulk contributions is shown along with the fits in the lower panels. For Sr 3*d*, a trend is observed: from STO crystal, going through the film on 0.05% substrate and to the film on 0.5% substrate, the amount of surface Sr systematically decreases. In turn, no clear trend is observed in the Ti 3*p* spectra with regard to the amount of Nb doping.

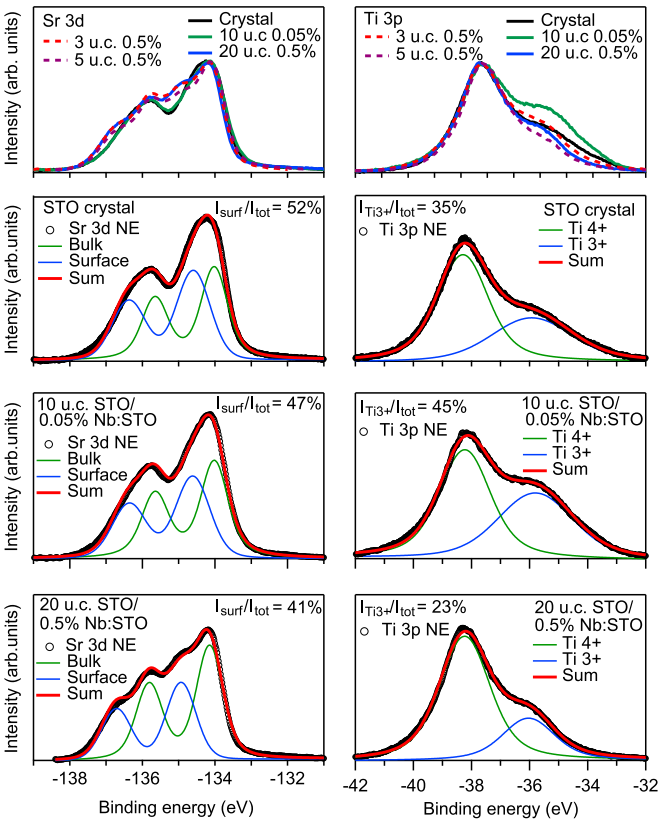

FIG. 14. Details of XPS fits. (a) Sr 3*d* and (b) Ti 3*p* spectra of different samples (top panel) and their fits (lower panels). The spectra of the 3 and 5 u.c. films is shown for comparison in dashed lines.

[1] N. Spaldin, S.-W. Cheong, and R. Ramesh, Phys. Today **63**(10), 38 (2010).

[2] N. Reyren, S. Thiel, A. D. Caviglia, L. F. Kourkoutis, G. Hammerl, C. Richter, C. W. Schneider, T. Kopp, A.-S. Rüetschi, D. Jaccard, M. Gabay, D. A. Muller, J.-M. Triscone, and J. Mannhart, Science **317**, 1196 (2007).

[3] J. A. Bert, B. Kalisky, C. Bell, M. Kim, Y. Hikita, H. Y. Hwang, and K. A. Moler, Nat. Phys. **7**, 767 (2011).

[4] Ariando, X. Wang, G. Baskaran, Z. Q. Liu, J. Huijben, J. B. Yi, A. Annadi, A. R. Barman, A. Rusydi, S. Dhar, Y. P. Feng, J. Ding, H. Hilgenkamp, and T. Venkatesan, Nat. Commun. **2**, 188 (2011).

[5] B. Kalisky, J. A. Bert, C. Bell, Y. Xie, H. K. Sato, M. Hosoda, Y. Hikita, H. Y. Hwang, and K. A. Moler, Nano Lett. **12**, 4055 (2012).

[6] A. Ohtomo and H. Hwang, Nature (London) **427**, 423 (2004).

[7] C. Cancellieri, M. L. Reinle-Schmitt, M. Kobayashi, V. N. Strocov, P. R. Willmott, D. Fontaine, P. Ghosez, A. Filippetti, P. Delugas, and V. Fiorentini, Phys. Rev. B **89**, 121412(R) (2014).

[8] N. C. Plumb and M. Radović, J. Phys.: Condens. Matter **29**, 433005 (2017).

[9] E. Frantzeskakis, T. C. Rödel, F. Fortuna, and A. F. Santander-Syro, J. Electron Spectrosc. Relat. Phenom. **219**, 16 (2017).

[10] A. F. Santander-Syro, O. Copie, T. Kondo, F. Fortuna, S. Pailhès, R. Weht, X. G. Qiu, F. Bertran, A. Nicolaou, A. Taleb-Ibrahimi, P. L. Fèvre, G. Herranz, M. Bibes, N. Reyren, Y. Apertet, P. Lecoeur, A. Barthélémy, and M. J. Rozenberg, Nature (London) **469**, 189 (2011).

[11] W. Meevasana, P. D. C. King, R. H. He, S.-K. Mo, M. Hashimoto, A. Tamai, P. Songsiriritthigul, F. Baumberger, and Z.-X. Shen, Nat. Mater. **10**, 114 (2011).

[12] N. C. Plumb, M. Salluzzo, E. Razzoli, M. Månsson, M. Falub, J. Krempasky, C. E. Matt, J. Chang, M. Schulte, J. Braun, H. Ebert, J. Minár, B. Delley, K.-J. Zhou, T. Schmitt, M. Shi, J. Mesot, L. Patthey, and M. Radović, Phys. Rev. Lett. **113**, 086801 (2014).

[13] S. M. Walker, F. Y. Bruno, Z. Wang, A. de la Torre, S. Riccó, A. Tamai, T. K. Kim, M. Hoesch, M. Shi, M. S. Bahramy, P. D. C. King, and F. Baumberger, Adv. Mater. **27**, 3894 (2015).

[14] S. N. Rebec, T. Jia, H. M. Sohail, M. Hashimoto, D. Lu, Z.-X. Shen, and R. G. Moore, Proc. Natl. Acad. Sci. USA **116**, 16687 (2019).

[15] P. Delugas, V. Fiorentini, A. Mattoni, and A. Filippetti, Phys. Rev. B **91**, 115315 (2015).

[16] A. D. Caviglia, M. Gabay, S. Gariglio, N. Reyren, C. Cancellieri, and J.-M. Triscone, Phys. Rev. Lett. **104**, 126803 (2010).

[17] M. J. Veit, R. Arras, B. J. Ramshaw, R. Pentcheva, and Y. Suzuki, Nat. Commun. **9**, 1458 (2018).

[18] A. F. Santander-Syro, F. Fortuna, C. Bareille, T. C. Rödel, G. Landolt, N. C. Plumb, J. H. Dil, and M. Radović, Nat. Mater. **13**, 1085 (2014).

[19] L. P. Gor'kov, J. Phys.: Condens. Matter **27**, 252001 (2015).

[20] A. C. Garcia-Castro, M. G. Vergniory, E. Bousquet, and A. H. Romero, Phys. Rev. B **93**, 045405 (2016).

[21] S. McKeown Walker, S. Riccò, F. Y. Bruno, A. de la Torre, A. Tamai, E. Golias, A. Varykhalov, D. Marchenko, M. Hoesch, M. S. Bahramy, P. D. C. King, J. Sánchez-Barriga, and F. Baumberger, Phys. Rev. B **93**, 245143 (2016).

[22] V. Mourik, K. Zuo, S. M. Frolov, S. R. Plissard, E. P. A. M. Bakkers, and L. P. Kouwenhoven, Science **336**, 1003 (2012).

[23] J. F. Schooley, W. R. Hosler, and M. L. Cohen, Phys. Rev. Lett. **12**, 474 (1964).

[24] K. Momma and F. Izumi, J. Appl. Crystallogr. **44**, 1272 (2011).

[25] Z. Wang, S. M. Walker, A. Tamai, Y. Wang, Z. Ristic, F. Y. Bruno, A. De La Torre, S. Riccò, N. Plumb, M. Shi, P. Hlawenka, J. Sánchez-Barriga, A. Varykhalov, T. Kim, M. Hoesch, P. King, W. Meevasana, U. Diebold, J. Mesot, B. Moritz, T. Devereaux, M. Radović, and F. Baumberger, Nat. Mater. **15**, 835 (2016).

[26] J. H. Dil, J. W. Kim, S. Gokhale, M. Tallarida, and K. Horn, Phys. Rev. B **70**, 045405 (2004).

[27] S. Ogawa, K. Kato, N. Nagatsuka, S. Ogura, and K. Fukutani, Phys. Rev. B **96**, 085303 (2017).

[28] P. Zhang, P. Richard, T. Qian, Y.-M. Xu, X. Dai, and H. Ding, Rev. Sci. Instrum. **82**, 043712 (2011).

[29] S. Moser, L. Moreschini, J. Jaćimović, O. S. Barišić, H. Berger, A. Magrez, Y. J. Chang, K. S. Kim, A. Bostwick, E. Rotenberg, L. Forró, and M. Grioni, Phys. Rev. Lett. **110**, 196403 (2013).

[30] P. D. C. King, S. McKeown Walker, A. Tamai, A. de la Torre, T. Eknapakul, P. Buaphet, S. K. Mo, W. Meevasana, M. S. Bahramy, and F. Baumberger, Nat. Commun. **5**, 3414 (2014).

[31] Y. S. Kim, J. Kim, S. J. Moon, W. S. Choi, Y. J. Chang, J.-G. Yoon, J. Yu, J.-S. Chung, and T. W. Noh, Appl. Phys. Lett. **94**, 202906 (2009).

[32] S. A. Chambers, Y. Du, Z. Zhu, J. Wang, M. J. Wahila, L. F. J. Piper, A. Prakash, J. Yue, B. Jalan, S. R. Spurgeon, D. M. Kepaptsoglou, Q. M. Ramasse, and P. V. Sushko, Phys. Rev. B **97**, 245204 (2018).

[33] M. Hoesch, T. Greber, V. N. Petrov, M. Muntwiler, M. Hengsberger, W. Auwaerter, and J. Osterwalder, J. Electron Spectrosc. Relat. Phenom. **124**, 263 (2002).

[34] J. H. Dil, Electron. Struct. **1**, 023001 (2019).

[35] F. Meier, J. H. Dil, and J. Osterwalder, New J. Phys. **11**, 125008 (2009).

[36] R. C. Hatch, K. D. Fredrickson, M. Choi, C. Lin, H. Seo, A. B. Posadas, and A. A. Demkov, J. Appl. Phys. **114**, 103710 (2013).

[37] A. Janotti, J. B. Varley, M. Choi, and C. G. Van de Walle, Phys. Rev. B **90**, 085202 (2014).

[38] X. Hao, Z. Wang, M. Schmid, U. Diebold, and C. Franchini, Phys. Rev. B **91**, 085204 (2015).

[39] I. Sokolović, M. Schmid, U. Diebold, and M. Setvin, Phys. Rev. Mater. **3**, 034407 (2019).

[40] M. Stengel, Phys. Rev. Lett. **106**, 136803 (2011).

[41] A. A. Sirenko, C. Bernhard, A. Golnik, A. M. Clark, J. Hao, W. Si, and X. X. Xi, Nature **404**, 373 (2000).

[42] T. Ostapchuk, J. Petzelt, V. Železný, A. Pashkin, J. Pokorný, I. Drbohlav, R. Kužel, D. Rafaja, B. P. Gorshunov, M. Dressel, C. Ohly, S. Hoffmann-Eifert, and R. Waser, Phys. Rev. B **66**, 235406 (2002).

[43] C. Cen, S. Thiel, G. Hammerl, C. Schneider, K. Andersen, C. Hellberg, J. Mannhart, and J. Levy, Nat. Mater. **7**, 298 (2008).

[44] V. N. Petrov, M. S. Galaktionov, and A. S. Kamochkin, Rev. Sci. Instrum. **72**, 3728 (2001).

[45] J. Yeh and I. Lindau, At. Data Nucl. Data Tables **32**, 1 (1985).